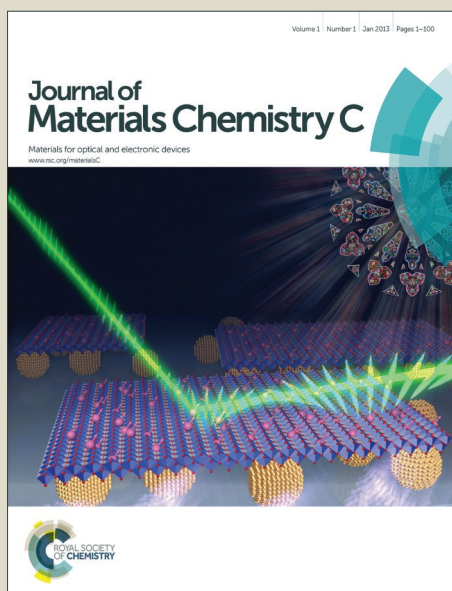


Journal of Materials Chemistry C

Accepted Manuscript



This is an *Accepted Manuscript*, which has been through the Royal Society of Chemistry peer review process and has been accepted for publication.

Accepted Manuscripts are published online shortly after acceptance, before technical editing, formatting and proof reading. Using this free service, authors can make their results available to the community, in citable form, before we publish the edited article. We will replace this *Accepted Manuscript* with the edited and formatted *Advance Article* as soon as it is available.

You can find more information about *Accepted Manuscripts* in the [Information for Authors](#).

Please note that technical editing may introduce minor changes to the text and/or graphics, which may alter content. The journal's standard [Terms & Conditions](#) and the [Ethical guidelines](#) still apply. In no event shall the Royal Society of Chemistry be held responsible for any errors or omissions in this *Accepted Manuscript* or any consequences arising from the use of any information it contains.

Cite this: DOI: 10.1039/c0xx00000x

ARTICLE TYPE

www.rsc.org/xxxxxx

Lead molybdate – a promising material for optoelectronics and photocatalysis

Przemysław Kwolek^{a,b}, Kacper Pilarczyk^{c,d}, Tomasz Tokarski^b, Marta Łapczyńska^e, Michał Pacia^f,
Konrad Szacilowski^{b,d,*}

Received (in XXX, XXX) XthXXXXXXXXXX 20XX, Accepted Xth XXXXXXXXXXXX 20XX

DOI: 10.1039/b000000x

The growing interest in the use of light as an information and energy carrier has led to the increased demand for new materials, characterised by particular photoelectrochemical properties. The aim of this work is the introduction of wide band gap semiconductor – PbMoO₄ with a detailed description of its synthesis procedure and products characterisation. The emphasis was put on its electronic structure and photoelectrochemical properties in order to evaluate the mechanism of the photoelectrochemical photocurrent switching effect (the PEPS effect). This phenomenon may be utilized in the construction of simple logic devices (e.g. logic gates or switches) or more complex optoelectronic circuits. Lead molybdate in the form of fine powder was obtained *via* a microwave assisted hydrothermal route. It was found that the composition of the reaction mixture (*i.e.* the ratio between lead and molybdate ions) influences the morphology and the electronic structure of the semiconductor. The photoelectrochemical characterization revealed that PbMoO₄ in the presence of Ce⁴⁺/Ce³⁺ redox couple exhibits the PEPS effect regardless of the presence of oxygen in the electrolyte. That may be explained in terms of oxidation/reduction processes of cerium(III)/cerium(IV) species. An attempt to modify the surface *via* the adsorption of alizarin onto PbMoO₄ was also made. The spectroscopic characterization and DFT calculations performed for such an organic-inorganic hybrid material revealed that the dye binds to Mo^{VI} centres which are exposed on the surface. Alizarin adsorbed onto PbMoO₄ strongly enhances the cathodic photocurrent generation. At the same time, however, the anodic photocurrent diminishes. Therefore, literally no switching effect occurs for such a system. Nonetheless, the generation of intense cathodic photocurrent may be utilized in the photocatalysis *e.g.* during the photoreduction of metal ions or the generation of reactive oxygen species and/or solar fuels.

Introduction

The rapid development of electronics requires new semiconducting and dielectric materials of superior quality. Recently, new applications induced the use of various organic materials as semiconductors, e.g. in thin layer field effect transistors. Transition metal oxides at their highest oxidation states usually exhibit semiconducting properties. The most notable example is titanium dioxide. The other oxides and oxide binary phases are also wide band gap semiconductors. These materials are usually studied from the point of view of the solid state chemistry or catalysis, but their semiconducting properties upon interaction with photosensitizers are not well studied with the notable exception of titanium dioxide. The application of these semiconductors as materials for switching devices is also not well recognized. One of such phases for which there is a significant lack of data on its semiconducting properties is lead molybdate.

It occurs in the Earth crust as mineral called wulfenite.¹ Single crystals of PbMoO₄ are commercially applied in manufacturing of acousto-optic modulators,² it is also a promising material for low temperature scintillators.³ Lead molybdate in the form of powder was examined towards photocatalytic decomposition of

water⁴⁻⁶ and mineralization of organic pollutants from wastewater.^{5, 7-12} Also heterostructures such as PbMoO₄/C₆₀ fullerene¹³ and TiO₂-N/Ag-PbMoO₄¹⁴ exhibit photocatalytic activity.

PbMoO₄ is mainly ionic compound which adopts tetragonal, scheelite-type crystal structure (space group *I4₁/a*). Such a structure is composed of MoO₄²⁻ tetrahedra which are linked *via* Pb²⁺ ions.¹⁵ The valence band near its edge is composed mainly of oxygen 2*p* and lead 6*s* orbitals. Molybdenum 4*d* and 5*d* states are involved in the formation of states deep below the valence band edge (around 3.5 eV). The conduction band in turn is dominated by Mo 5*d* states with the admixture of Pb 6*p* orbitals. The contribution of Pb 6*s* in this band is insignificant. Similarly, the contribution of lead 5*s* and 5*p* in both energy bands can be neglected. The semiconducting properties of PbMoO₄ arise due to the interactions between Mo *d* states with O 2*p* orbitals which gives some covalent contribution to the ionic bonds.¹⁵⁻¹⁸ The value of the band gap determined experimentally lies between 3.1 and 3.4 eV,^{5, 8, 18-20} whereas calculations give much wider energy range *i.e.* from 2.6 eV to 4.8 eV. The character of the band-to-band transition is indirect.¹⁵⁻¹⁸

The sign of majority charge carriers depends strongly on the presence of lattice defects which are either oxygen or lead vacancies.²¹ Hence, the type of conductivity may be affected by

the annealing conditions, particularly oxygen pressure.²² There is only one experimental work concerning the type of conductivity of this compound. Nam *et al.*, based on the photoelectrochemical measurements, concluded that PbMoO₄ is *p*-type semiconductor.⁶

Despite the fact that for the commercial applications lead molybdate is obtained in the form of single crystals using Bridgman and Czochralski techniques,^{9, 22} there are plenty of synthesis methods which enable obtaining PbMoO₄ in the form of fine powder. The simplest procedure is based on its precipitation from the solution containing lead and molybdate ions^{23, 24} and is commercially used for Mo recovery from disposed Ni - Mo catalysts.²⁵ Lead molybdate is commonly synthesized *via* a hydrothermal and solvothermal routes,^{5, 7, 11-13, 18, 19, 26} which often include either heating of the reaction mixture by microwave irradiation²⁷ or sonochemical preparation.^{14, 28, 29} The morphology of the product may be controlled primarily by the changes in the composition of the reaction mixture *i.e.* the ratio of Pb²⁺ and MoO₄²⁻ concentrations, but also *via* the addition of surfactants and appropriate selection of the hydrothermal treatment temperature.⁵ The product is usually obtained in the form of polyhedra^{7, 18-20} and nanorods.^{8, 26-28}

Experimental

The synthesis was performed in a microwave heated, high pressure autoclave Magnum II (Ertec, Poland). Lead acetate (Pb(CH₃COO)₂·3H₂O, Sigma Aldrich) and sodium molybdate (Na₂MoO₄·2H₂O, POCH) were dissolved in deionized water. Lead acetate solution was acidified with acetic acid to prevent hydrolysis. The total volume of the reaction mixture was 40 cm³ and pH was equal to 4. Immediately after mixing both solutions lead molybdate precipitates. Its solubility product is equal to 1.2·10⁻¹³.³⁰ The reaction mixture was then transferred to a Teflon vessel and heated using microwave irradiation for 1 hour (according to the procedure described in our previous work).³¹ The influence of the temperature on the morphology and the electronic structure of the product was determined. The detailed information on the synthesis conditions are given in Table 1.

Table 1. The parameters of the synthesis.

	aliquot of Pb(CH ₃ COO) ₂ ·3H ₂ O / g	aliquot of Na ₂ MoO ₄ ·2H ₂ O / g	Conditions	
			T / K	P / bar
1a	0.8707	0.6592	438	9-12
2a	0.8710	0.6591	468	19-22
3a	0.8713	0.6587	493	29-32
4a	0.8714	0.6589	518	39-42
1b	1.0328	0.6599	443	9-12
2b	1.0336	0.6595	463	19-22
3b	1.0328	0.6599	495	29-32
4b	1.0336	0.6595	523	39-42
1c	1.0223	0.5594	448	9-12
2c	1.0333	0.5595	453	19-22
3c	1.0333	0.5594	486	29-32
4c	1.0333	0.5594	513	39-42

The samples from **1a** - **4a** were obtained with the deficiency of Pb²⁺ ions in the reaction mixture (85% of the stoichiometric amount), **1b** - **4b** - with the stoichiometric composition and **1c** - **4c** with the MoO₄²⁻ deficiency (85% of the stoichiometric amount). The precipitate was washed several times with deionized water, centrifuged and dried in air.

The sample **1b** was modified by the adsorption of alizarin. The modifier was dissolved in isopropyl alcohol and sonicated with the powder, then centrifuged. The change in colour of the

material was observed from white to purple due to alizarin adsorption. In order to remove excess of the dye from PbMoO₄ surface, the precipitate was washed several times with the solvent, centrifuged and finally dried in air.

The diffuse reflectance spectra were recorded on Lambda 950 (Perkin Elmer, USA) spectrophotometer equipped with 150 mm integration sphere. The sample was dispersed in spectrally pure BaSO₄ in 1:50 weight ratio. Pressed BaSO₄ pellet was used as a reference. The photoluminescence spectra were recorded on Fluoromax 4P spectrofluorimeter (Horiba Jobin Yvon, France). The sample (0.4 mg) was dispersed in 100 cm³ of deionized water using ultrasonic bath and excited at different wavelengths. The electrochemical impedance spectra were measured on SP-300 potentiostat (Bio-Logic, France) in deoxygenated 0.1M KCl solution at pH = 5. The working electrode was prepared by the deposition of neat or modified PbMoO₄ onto indium-tin oxide (ITO) coated polyethylene terephthalate foil. The powder was carefully grated in a mortar with a small amount of water. Subsequently, PET substrate was painted with the slurry using a pestle. Finally, the electrode was gently dried in air. In the case of PbMoO₄ the described procedure allows the preparation of well adherent layer which stayed unchanged in the electrolyte during the electrochemical experiments. It was observed that the smaller semiconductor grains the easier obtaining of good quality electrode.

The photoelectrochemical characterization was performed using a photoelectric spectrometer (Instytut Fotonowy, Poland) composed of stabilized 150 W xenon arc lamp, monochromator and coupled with the SP-300 potentiostat. Simultaneously, the photocatalytic activity of the obtained materials was tested. All the experiments were done under the same conditions, using the 150 W xenon arc lamp. NIR filter (0.1M CuSO₄ water solution) and a bandpass 300–500 nm filter were used to prevent heating of the sample and the excitation of Azure B itself. Under these conditions Azure B is stable.³² PbMoO₄ was suspended in a model pollution solution (Azure B, 24.34 μM, the absorbance at 646 nm equal to 1.000). The final concentration of lead molybdate was 1 g·dm⁻³. The suspension was sonicated for 30 minutes and irradiated in optical glass cuvette (5 cm diameter, 1 cm optical path, 17 mL volume) for 1 hour. Then, the samples were collected and centrifuged for 20 minutes at 10 000 RPM. The absorption spectrum of the supernatant was recorded on HP 8453 UV-Vis spectrophotometer in the 1 cm quartz cuvette. The degradation of Azure B was calculated from the absorption changes at 646 nm band.

The quantum-chemical modelling was performed in AGH Computing Centre CYFRONET using Gaussian 09 Rev. A.02 at the B3LYP/SDD level of theory.³³ The application of SDD basis enabled reliable computation of heavy ion behaviour.³⁴ The powder diffraction pattern was simulated with Mercury 3.3 software (The Cambridge Crystallographic Data Centre, 2013).

Results and discussion

Crystal structure and morphology

Lead molybdate was obtained in the form of fine, white powder. First of all, the powder X-ray diffraction measurements were performed to confirm the crystal structure of the product. The analysis of the recorded diffractograms indicates that regardless of the synthesis temperature the material possess tetragonal crystal structure, which is characteristic for wulfenite¹⁵ (space group I41/a, ICDD PDF 2010 Fig. 1). No significant impurities were found in the sample.

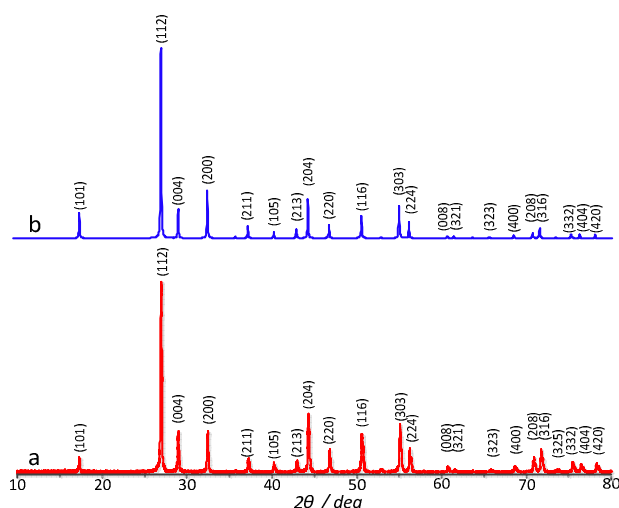


Fig. 1. The X-ray diffraction pattern recorded for the sample 4a revealing the crystal structure of the synthesised product (tetragonal, space group I41/a) with no impurities (a). A simulated diffraction pattern based on natural wulfenite single crystal structure³⁵ is shown for comparison (b).

Since PbMoO_4 was obtained either in the form of very fine powder (below 100 nm in diameter) or almost 100 times bigger microcrystals, in the first case the obtained diffraction peaks were characterised by a greater width at half maximum and the significant increase of background signal (due to lower crystallinity) was observed. It should be noted that in all the cases polydisperse material was obtained with typical width at half height from 30 nm for the finest nanopowders to ca. 1000 nm for microcrystalline samples.

It is noteworthy that a correlation between synthesis conditions and the morphology of PbMoO_4 powder was found. In the case when the reaction mixture was deficient of Pb^{2+} ions, the size of crystals gradually increased with the increasing temperature of the hydrothermal treatment. At 438 K two distinctive fractions were observed *i.e.* nanocrystals with the average diameter of ca. 80 nm and some microcrystalline material of ca. 690 nm in diameter. However, the higher the temperature was, the lower the content of finer grains and above 493 K only microscopic crystals were observed. At the same time, for the stoichiometric composition there was a stronger tendency towards formation of a nanopowder. The grains were smaller (average diameter of ca. 52 nm) and their average size increased with the temperature up to ca. 86 nm at 495 K. For this sample some microcrystals with the diameter of approx. 560 nm were also found. At higher temperatures only microcrystalline phase was stable. Finally, when there was an excess of Pb^{2+} in the reaction mixture, only nanocrystals were formed in the whole temperature range. Their size slightly increased with the temperature from ca. 49 nm for 448 K to 57 nm for 513 K in diameter (Fig. 2). The mechanism responsible for this change in crystals morphology is probably Oswald ripening. What is more, the lower temperature and the higher concentration of Pb^{2+} in the reaction mixture were, the narrower distribution of the grain sizes was observed (Fig. 3, see also ESI for details). The correlation between the temperature of the hydrothermal treatment and the grain diameter is summarized in Fig. 2.

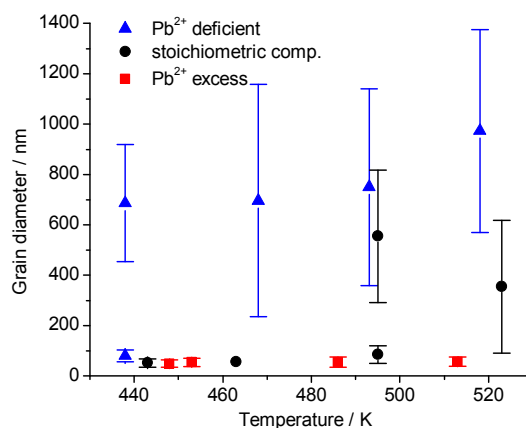


Fig. 2. The variation of average grain diameter with the temperature changes for different compositions of the reaction mixture.

45 Spectroscopic characterization

Subsequently, the diffuse reflectance spectroscopy was used to characterize spectroscopic properties of the obtained material.³⁶ The Kubelka–Munk function f^{KM} was calculated using formula (1):

$$f^{KM} = \frac{(1-R(h\nu))^2}{2R(h\nu)} = \frac{\alpha(h\nu)}{S} \quad (1)$$

where $R(h\nu)$ is the reflectance of the sample measured vs. BaSO_4 pellet (100% reflectivity standard), $\alpha(h\nu)$ is the absorption coefficient and S is the scattering factor. The latter is usually treated as a wavelength independent and is equal to the scattering factor for barium sulphate. Practically, Kubelka–Munk formula is regarded as valid for the absorbing layer which is at least 3 mm thick.³⁶ Afterwards, the value of the forbidden band width was determined using the Tauc plots. It was proved, through the analysis of DFT calculations results,^{15–18} that PbMoO_4 is an indirect band gap semiconductor. In that case the equation given below may be applied (2).³⁷

$$(f^{KM} h\nu)^{1/2} = A(h\nu - E_g) \quad (2)$$

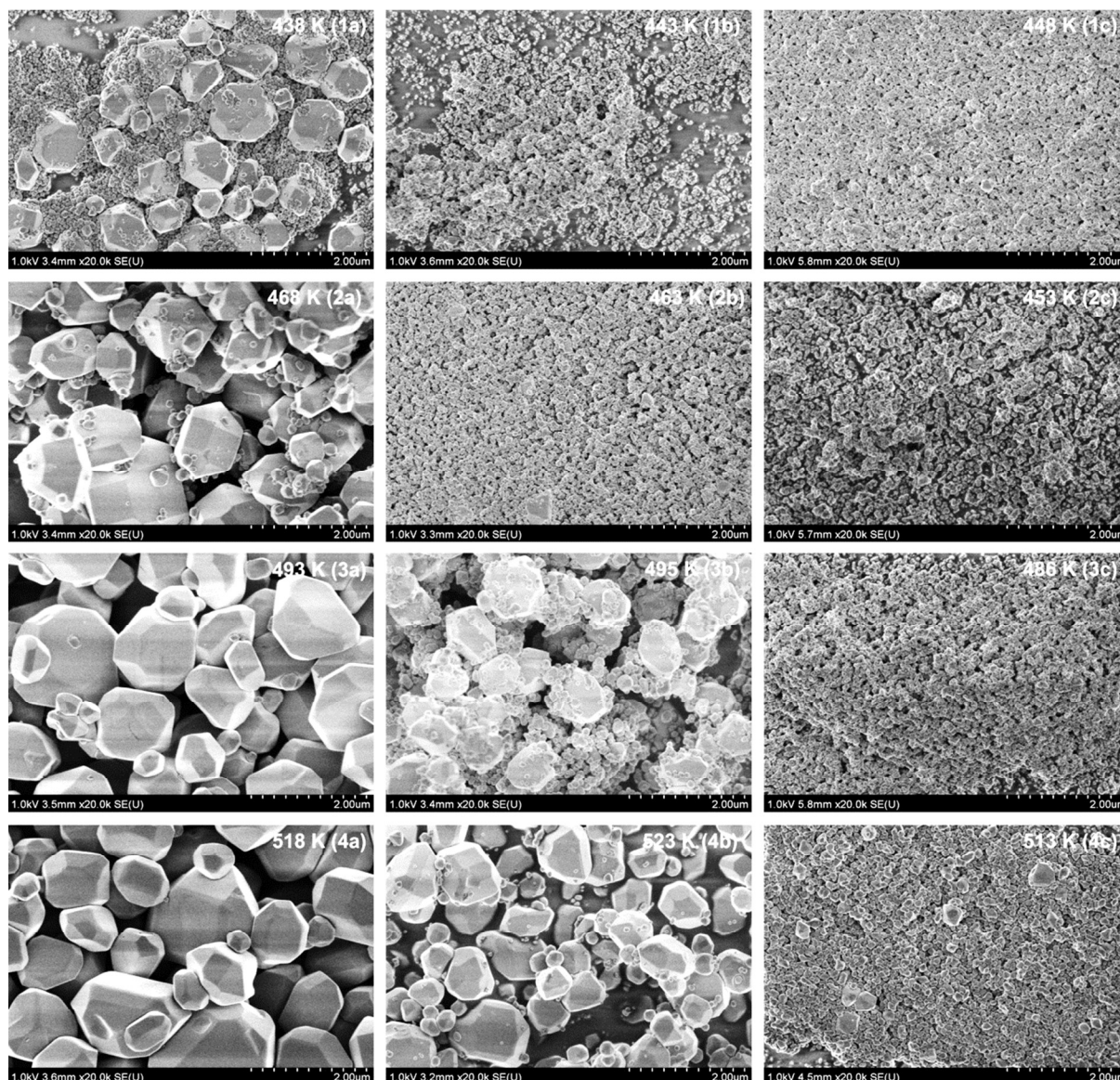


Fig. 3. The morphology of PbMoO_4 obtained at various temperatures of the hydrothermal treatment for Pb^{2+} deficient reaction mixture (a), stoichiometric composition (b) and the excess of Pb^{2+} in the reaction mixture (c).

The spectroscopic characterization indicated that E_g value depends on the temperature of the hydrothermal treatment *i.e.* the lower Pb^{2+} content in the reaction mixture and lower temperature, the wider is the band gap as it is presented in Fig. 4. Moreover, the average grain diameter depends on the synthesis conditions in the same manner (Fig. 2). Therefore, the correlation between the forbidden band width and the size of the crystals can be seen in the whole range of the observed grain sizes (Fig. 5). For the excess of Pb^{2+} ions only grains below 60 nm were formed. Relatively small increase in the diameter (from 49.3 to 57.2 nm) connected with the rising temperature results in the decrease of the E_g value. A stronger dependence may be observed for the stoichiometric composition of the reaction mixture, where both ca. 50 nm and 355 nm crystals were obtained depending on the temperature of the hydrothermal treatment. In this case, the decrease in the energy gap width related to the increasing grain diameter is more evident. When the reaction mixture was depleted of Pb^{2+} ions the increase of the E_g value was observed only for the lowest temperature and the grain size was below 80

nm. In the range between 700 and 1000 nm the band gap width is virtually insensitive to the changes in the average grain size. Thus, one may conclude that weak quantum confinement is directly responsible for the observed increase in the forbidden gap width in the case of smaller crystals. This conclusion was further verified by the fitting of the Brus equation³⁸ (3) to the experimental data. This equation related the band gap of nanocrystals (E_r) with the bulk band gap and average nanoparticle diameter (d), where m_e^* and m_h^* are effective masses of electrons and holes, respectively, e is the elementary charge and ϵ is the vacuum permittivity. The fitted band gap energy of 3.29 ± 0.01 eV is fairly consistent with the reported value of optical band gap for this material (3.2 eV).³⁹

$$E_r = E_g + \frac{\hbar^2 \pi^2}{8d^2} \left(\frac{1}{m_e^*} + \frac{1}{m_h^*} \right) - \frac{0.9e^2}{\epsilon d} \quad (3)$$

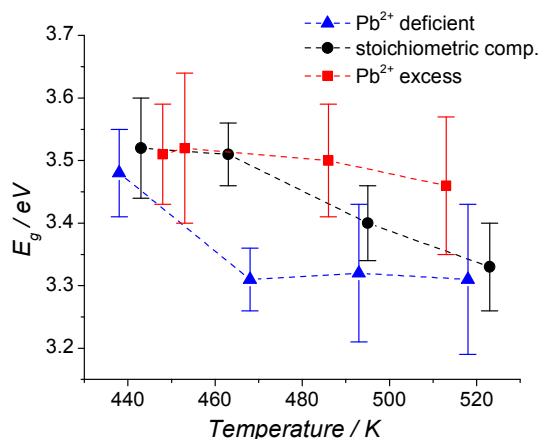


Fig. 4. The band gap dependence on the temperature of the hydrothermal treatment for different compositions of the reaction mixture. For reasons of clarity the data points obtained for the same composition of the reaction mixture were connected with the dash line.

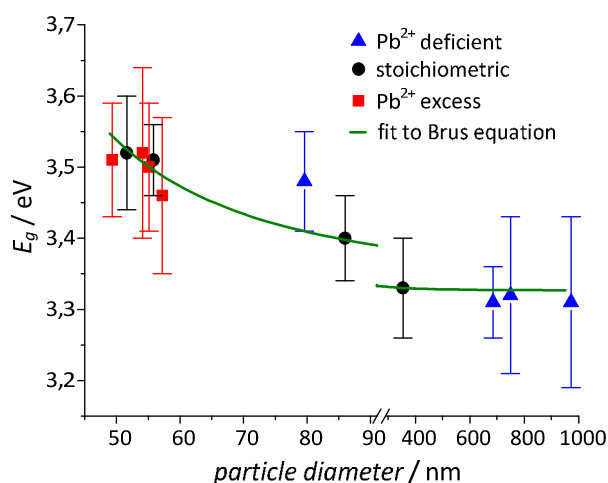


Fig. 5. The correlation between the band gap width and the average grain diameter for different compositions of the reaction mixture suggesting the occurrence of the weak quantum confinement.

10 Apart from the determination of the band gap width, also the low-energy part of the reflectance spectra *i.e.* the Urbach tails region was analysed. The exponential growth of the absorption coefficient value with the increase of incident photon energy ($h\nu$) below the absorption edge may be described as follows (4):

$$15 \quad f^{KM} = \alpha_0 \exp\left(\frac{h\nu - E_0}{E_U}\right) \quad (4)$$

where E_U is the Urbach energy connected with the thermal distortion and structural disorder in the lattice.⁴⁰ The Urbach energy values were determined for each sample as the inversion of the linear function slope fitted to $\ln f^{KM}$ plotted vs. incident photon energy ($h\nu$). The obtained results are presented in Fig. 6.

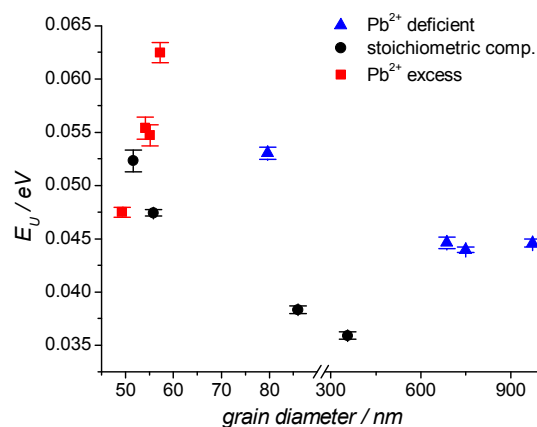


Fig. 6. The Urbach energy as a function of average grain diameter of the synthesised powder.

One may conclude that for both stoichiometric composition and for the excess of molybdate ions present in the reaction mixture, the Urbach energy values decrease gradually with the increasing grain size. It is not surprising, since the bigger crystals were obtained at the higher temperature of the hydrothermal treatment which also led to a higher degree of the product crystallinity. The increase in temperature (and also in the grain diameter) reduces the Urbach energy only to some extent – its value still oscillates around 45 meV in the case of MoO₄²⁻ excess. E_U represents the influence of both structural disorder and thermal fluctuations associated with phonons as expressed by the equation (5):⁴⁰

$$E_U = \frac{E_p}{2\sigma_0} \left(X + \coth \frac{E_p}{2k_B T} \right) \quad (5)$$

where E_p is the energy of phonon in the lattice, σ_0 describes the ionicity of the crystal lattice, X is the ratio of the mean square deviation of the atomic position from its zero-point energy value and is related exclusively with the structural disorder. Thus, for the ideal crystals of a sufficient size, the Urbach energy approaches the value characteristic for the thermal distortion only. In the case of the stoichiometric composition of the reaction mixture, the Urbach energy leveling off with increasing temperature was not observed, probably due to the size of the grains which were smaller than in the previous case. Except for the first sample obtained at the lowest temperature, stoichiometric composition of the reaction mixture enables obtaining the lowest Urbach energies which means the lowest structural and thermal disorder. Only the samples synthesized with the excess of Pb²⁺ ions do not follow the described correlation. It suggests that in this case the temperature increase not necessarily improves the crystallinity of the powder. As matter of fact, all the samples obtained under such synthesis conditions are characterized by similar grains diameters, whereas for molybdate excess both 80 nm and ten times bigger structures were obtained. The prolongation of the hydrothermal treatment may lead to much bigger grains and associated decrease in the Urbach energy value.

The values of the band gap width were confirmed with the results of the fluorescence spectroscopy (Fig. 7). One may notice that for the larger grain diameters (*i.e.* from 555 to 972 nm - samples **3b**, **4b**, **2a**, **3a**, **4a**) the peak related to the radiative band-to-band transition is broad and its intensity is relatively low. For the powders characterised by the grain size below 80 nm

(samples **1a**, **1b**, **2b** and **1-4c**) this peak is more intense and sharper. This observation indirectly confirms the hypothesis of a weak quantum confinement. For coarse grains the electronic structure is well defined, hence the very broad emission band characteristic for bulk semiconductors is observed. At the same time, the reduction in the grain size distorts the electronic structure in such a way that band gap width increases while the energy levels constituting the valence and conduction bands become separated and the narrowing of the luminescent peak is observed as the consequence. The peak centred at 3 eV recorded for the sample **3b** arises probably from the energy transfer process occurring between grains of different sizes.

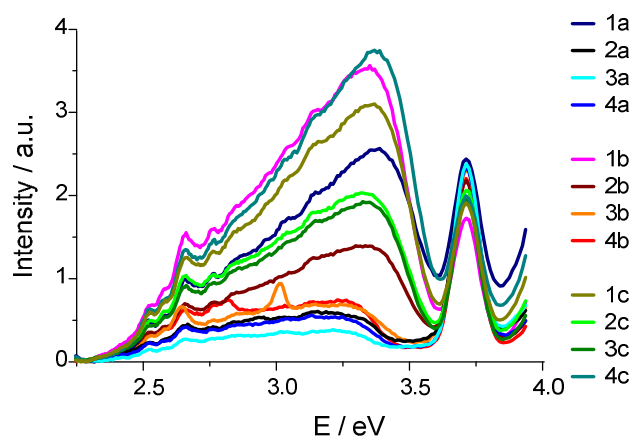


Fig. 7. The photoluminescence spectra of PbMoO_4 samples measured in water suspension. Samples were excited at 300 nm.

In order to estimate the conduction band edge potential, The Mott-Schottky analysis of measured EIS spectra was carried out. In the first step, the quality of the spectra was confirmed with the Kramers – Kronig transformation.^{41, 42} EIS spectra were recorded potentiostatically from 200 kHz to 1 Hz in the potential range between 1.25 and 0.05 V vs. SHE. Then, the impedance of a simple equivalent circuit *i.e.* resistor connected in series with constant phase element (CPE) was fitted to the measured impedance spectra and resistance R as well as Q and α parameters characterising the CPE element were determined. The impedance of CPE is described as follows(6):⁴³

$$Z_{\text{CPE}} = \frac{1}{Q(j\omega)^\alpha} \quad (6)$$

where ω is the angular frequency. The capacitance C was calculated using the formula (7):⁴³

$$C = Q^\alpha R \frac{1-\alpha}{\alpha} \quad (7)$$

this equation is valid, when the α coefficient is higher than 0.9. Knowing the capacitance it is easy to calculate the flatband potential E_{fb} using the Mott-Schottky equation (8):⁴³

$$\frac{1}{C^2} = \frac{2}{\epsilon\epsilon_0 e N_D} \left(V - V_{fb} - \frac{k_B T}{e} \right) \quad (8)$$

where ϵ stands for the dielectric constant of the sample, ϵ_0 is the vacuum permittivity, e is the elementary charge, N_D – the donor atoms density, k_B – the Boltzmann constant and T – the temperature. The obtained value is virtually equal to the conduction band edge potential for the n – type semiconductor.

The detailed calculation procedure was described in our previous publication.⁴⁴

It may be concluded that the conduction band edge potential determined for each sample does not depend on the synthesis conditions and is averagely equal to -0.14 ± 0.07 V vs. SHE. The conductivity type of the material was identified as n – type from the slope of the Mott - Schottky plot. It is, at the same time, in contrast with the work of Nam *et al.*,⁶ where they found in the photoelectrochemical measurements that their sample was the p -type semiconductor. The discrepancy may be caused by different nature of defects present in the crystalline structure.

The obtained nanopowder (the sample obtained at stoichiometric composition and lowest temperature) was also modified by the adsorption of alizarin. Such a surface treatment alters not only spectroscopic properties of material but also should affect photoelectrochemical properties. The change in absorption and photocurrent action spectra should depend on the mechanism of electron transfer between semiconducting nanoparticle and organic molecule *i.e.* optical electron transfer (OET) in the case of a strong interaction between both counterparts and photoinduced electron transfer (PET) for a weak interaction. Alizarin adsorbed on wide band gap semiconductors is usually involved in PET process due to relatively low energy of the intramolecular charge transfer process. This kind of behaviour is usually accompanied with relatively small changes in absorption spectrum of the dye (bathochromic shift due to the interaction with metal centre). The absorption spectra of such a hybrid material are compared with pure dye and unmodified semiconductor in Fig. 8.

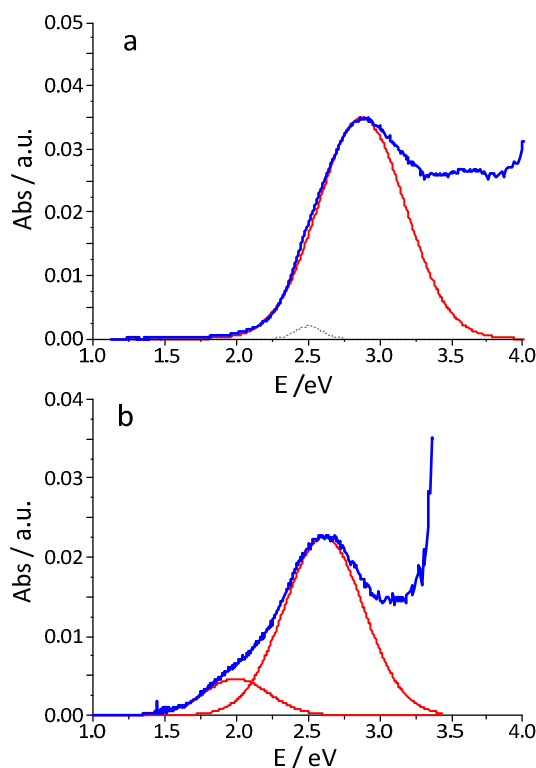


Fig. 8. The reflection spectra of alizarin adsorbed onto BaSO_4 (a) and onto PbMoO_4 (b).

Alizarin adsorbed at the surface of BaSO_4 shows one absorption band in the visible range at 2.88 eV, which is consistent with previous reports. This band is associated with a HOMO-LUMO transition of intramolecular charge transfer

character.⁴⁵ Minor transition at ca. 2.5 eV is associated with the presence of a small fraction of a tautomeric form of the dye.⁴⁵ Upon chemisorption at the PbMoO₄ surface the spectral properties of the dye are changed. The main transition is bathochromically shifted to 2.61 eV and a new spectral feature at 2.00 eV can be observed. This new band must originate from interactions between alizarin and surface molybdenum or lead ions. In order to assign the proper bonding mode a simplified theoretical model was built (Fig. 9) and the absorption spectra calculated using the TD-DFT approach at the B3LYP/SDD level of theory were compared with the calculated electronic spectrum of alizarin. It was found that the interaction with Pb²⁺ cation results in a minor bathochromic shift (HOMO→LUMO transition at 2.61 eV vs. 2.64 eV for a free dye molecule). On the other hand the interaction with MoO₄²⁻ results in two transitions in the visible range: at 2.11 and 2.31 eV. These two transitions, of dominating HOMO→LUMO and HOMO-1→LUMO character, respectively, are of a ligand-to-metal charge transfer (LMCT) character (Fig. 10). In these transitions alizarin plays a role of electron donor, while molybdate anion is an electron acceptor. This result indicates that surface molybdate anions are primary binding sites for alizarin and that the photosensitization processes in the alizarin-PbMoO₄ are most probably of OET character. This is an exception from the reported properties of alizarin at titanium dioxide surfaces.^{46, 47}

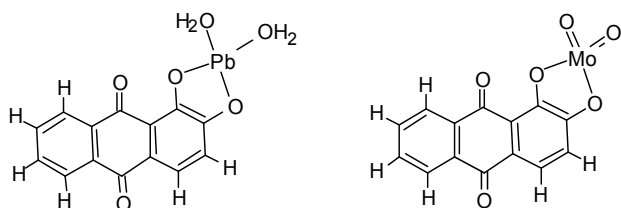


Fig. 9. The computational models of alizarin complexes with lead cations and molybdate anion.

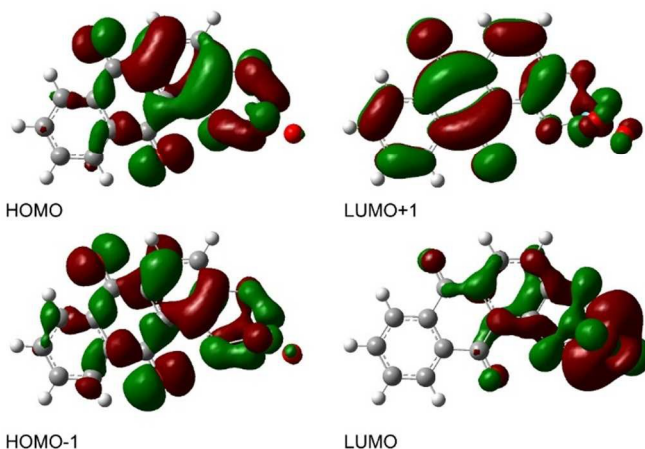


Fig. 10. The frontier orbitals of model alizarin-molybdate complex calculated using the rb3lyp/sdd level of theory.

Photoelectrochemical characterization

Since semiconducting nanostructures have become commonly used in optoelectronic and photovoltaic devices, the investigation of their photoelectrochemical properties gains importance nowadays. The information on these parameters enables the utilization of semiconductors nanoparticles in solar fuel cells, photocatalytic systems,⁴⁸ information processing devices⁴⁹ and even hydrometallurgy.⁵⁰ The Photoelectrochemical Photocurrent

Switching Effect (the PEPS effect), which may be defined as an ability of semiconductor to generate either anodic or cathodic photocurrents depending on the stimulus (the wavelength of the incident light or the electrode potential) is interesting from the information processing viewpoint. On the other hand, the suitable value of the conduction band edge potential gives the opportunity to use this material for the generation of the reactive oxygen species (ROS).

The photoelectrochemical properties of PbMoO₄ were measured with the help of the pulsed photocurrent spectroscopy. Since water molecules and/or hydroxyl ions present in the electrolyte often scavenge holes insufficiently,⁴⁴ Ce⁴⁺/Ce³⁺ redox couple was introduced in the photoelectrochemical experiment to avoid the possible photocorrosion of the electrode. The standard redox potential of this couple is equal to 1.72 V vs. SHE.⁵¹ Thus, ΔG of Ce³⁺ oxidation process with a hole from the valence band amounts to -152.5 kJ/mol. In the presence of cerium ions, the PEPS effect was observed. The switching potential *i.e.* the potential value for which anodic-to-cathodic (or *vice versa*) photocurrent transition occurs is equal to ca. 0.6 V vs. SHE and is independent of the presence of the molecular oxygen in the electrolyte. The reduction of oxygen dissolved in the electrolyte is a common cause of the cathodic photocurrent generation for the *n*-type semiconductors.⁵² Since the switching potential does not depend on the presence of molecular oxygen in the electrolyte, the reduction of Ce⁴⁺ ions with electrons from the conduction band is entirely responsible for the generation of cathodic photocurrent (Fig. 11).

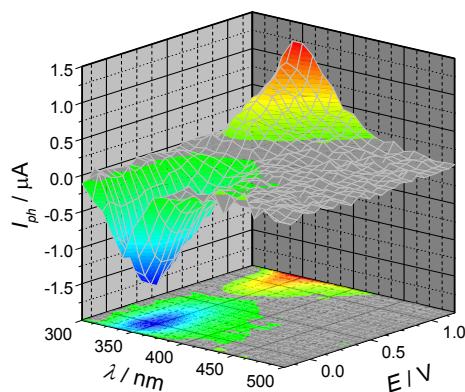


Fig. 11. The photocurrent action spectra of the sample **1b** recorded for various electrode potentials in 0.1M KNO₃ with 10 mM Ce³⁺ ions under anaerobic conditions.

Although the value of the standard reduction potential of the Ce⁴⁺/Ce³⁺ redox couple is significantly different than the observed switching potential, the kinetics of the Ce⁴⁺ ions reduction is relatively slow and the reaction takes place with a substantial overpotential.⁵³ Moreover, in the presence of excess of NO₃⁻, both Ce³⁺ and Ce⁴⁺ ions can exist in the complexed form, which additionally affects the redox process. It is noteworthy, that the kinetics depends also on the working electrode material.⁵⁴ The explanation of the PEPS effect mechanism for the described system is summarized in Fig. 12.

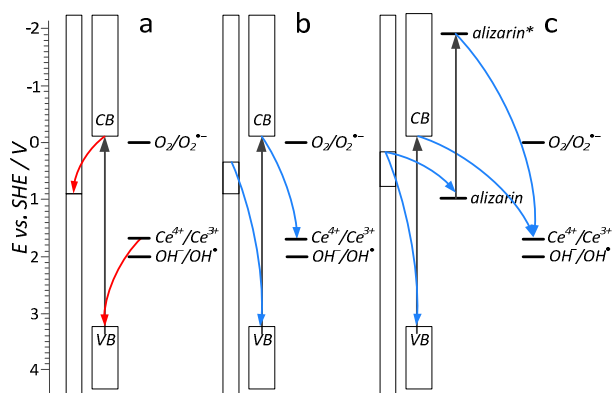


Fig. 12. The energy diagram illustrating the mechanism of anodic (a) and cathodic (b) photocurrents generation in the presence of Ce^{4+}/Ce^{3+} redox couple for unmodified material and for $PbMoO_4$ modified by the adsorption of alizarin (c).

As it was shown, the adsorption of alizarin onto lead molybdate surface strongly alters the spectroscopic properties of the material. It also drastically changes its photoelectrochemical properties. Namely, the cathodic photocurrent was observed almost exclusively in the whole potential range regardless of the presence of oxygen in the electrolyte (Fig. 13). The experiment was performed in the narrower (compared to the previous results) potential window due to the instability of alizarin above 0.8 V vs. SHE. The mechanism of such a strong enhancement of cathodic photocurrent may be probably explained in terms of the Ce^{4+} ions reduction with electrons originating from the alizarin excitation (Fig. 12c). The molecule of alizarin can be divided into two parts: the quinone moieties behave as the electron acceptors, whereas phenyl groups play the role of electron donors. Such inhomogeneous charge distribution within the organic layer deposited onto semiconducting particle may also enhance the electron transfer from the conduction band to the electron acceptor present in the electrolyte.⁴⁵ The recorded photocurrent action spectra revealed also only minor photosensitization at the negative polarization of the photoelectrode.

The results of the evaluation of $PbMoO_4$ photocatalytic activity are shown in Fig. 14. One may see that all materials are photoactive in the nonselective process of Azure B degradation. The highest activity was obtained for the Pb-rich materials. What is more, it significantly increases with the temperature of synthesis. It should be noted that the grain size of these samples is the lowest (the highest surface area) and virtually remains constant with the temperature changes. Similar dependence was observed for the samples prepared at stoichiometric composition of the reaction mixture. However, in this case photocatalytic activity is lower, probably due to the increasing content of larger grains (Fig. 3) which translates into a decrease in the surface area. One may conclude that decreasing Pb content in the reaction mixture lowers its photocatalytic activity. In the case of Pb-deficient samples, increasing temperature causes slight deterioration of photocatalytic activity.

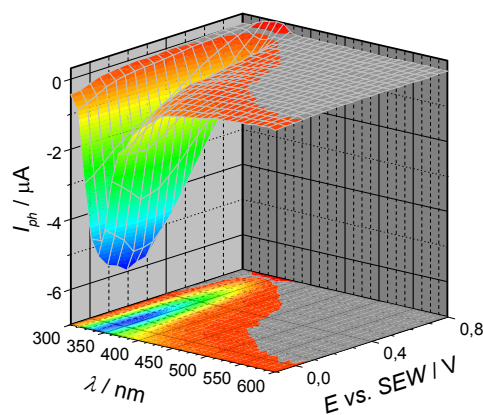


Fig. 13. The photocurrent action spectra of the sample **1b** modified with 45 alizarin recorded for various electrode potentials in 0.1M KNO_3 with 10 mM of Ce^{3+} ions under anaerobic conditions.

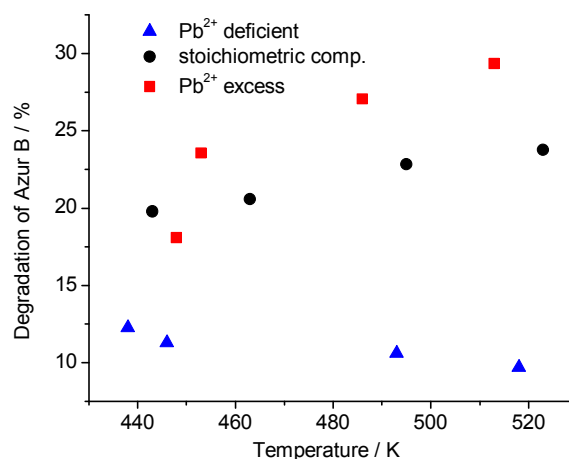


Fig. 14. The degradation of Azure B with the temperature changes for different compositions of the reaction mixture.

50 Conclusions

Lead molybdate was obtained *via* the hydrothermal method which is straightforward and environmentally friendly. The product was obtained in the form of nano- or micropowder. It was shown that both the morphology and the electronic structure (*i.e.* the value of the band gap width) may be tuned – to some extent – by an appropriate modification of the synthesis conditions. It was proven that the higher temperature and the lower Pb^{2+} content in the reaction mixture were, the bigger grains of the powder and lower values of the energy gap were obtained. The surface modification of $PbMoO_4$ *via* alizarin adsorption does not result in photosensitization. The dye is bonded mainly to the molybdenum ions exposed at the surface.

The photoelectrochemical characterization of the material revealed that in the presence of appropriate electron donor-acceptor system (*e.g.* Ce^{4+}/Ce^{3+} redox couple) in the electrolyte, the photoelectrochemical photocurrent switching effect may be induced. On the one hand, the adsorption of alizarin onto $PbMoO_4$ surface leads to a very efficient generation of cathodic photocurrent which may be effectively utilized in the photocatalytic applications, such as the photoreduction of metals from wastewater⁵⁰ or the reactive oxygen species (ROS)

generation for water purification purposes. The materials exhibits also a notable photocatalytic activity towards mineralization of organic pollutants which strongly depends on the synthetic conditions.

5 On the other hand, the PEPS effect observed in the described system constitutes a fundament for the construction of molecular logic devices and the further exploration of such a phenomenon may be interesting from the point of view of the optoelectronics and information processing.⁴⁹

10 Acknowledgment

Financial support from the Ministry of Science and Higher Education (grant no. IP2012 030772), National Science Centre (grants no. UMO-2012/05/N/ST5/00327 and UMO-2011/03/B/ST5/01495) and from the Foundation for Polish Science (grant no. TEAM/2012-9/4) is gratefully acknowledged.

Notes and references

^aDepartment of Materials Science, Rzeszow University of Technology, ul. W. Pola 2, 35-959 Rzeszów, Poland

^bAGH University of Science and Technology, Faculty of Non-Ferrous Metals, al. A. Mickiewicza 30, 30-059 Kraków, Poland; E-mail: szacilow@agh.edu.pl

^cAGH University of Science and Technology, Faculty of Physics and Applied Computer Science, al. A. Mickiewicza 30, 30-059 Kraków, Poland

^dAGH University of Science and Technology, Academic Centre for Materials and Nanotechnology, al. A. Mickiewicza 30, 30-059 Kraków, Poland

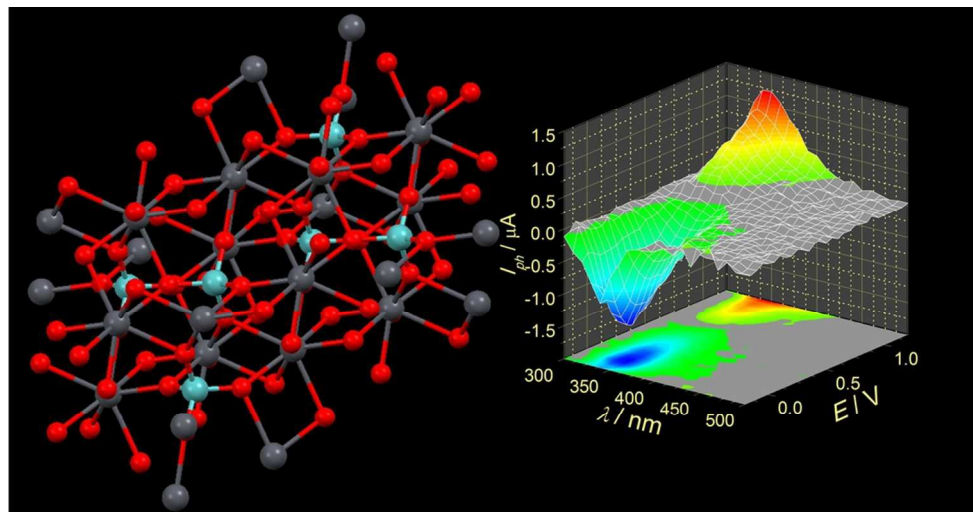
^eJerzy Haber Institute of Catalysis and Surface Chemistry Polish Academy of Sciences Niezapominajek 8, 30-239 Kraków, Poland

^fFaculty of Chemistry, Jagiellonian University, Ingardena 3, 30-060 Kraków

† Electronic Supplementary Information (ESI) available: [details of any supplementary information available should be included here]. See DOI: 10.1039/b000000x/

1. J. Leciejewicz, *Z. Kristallogr.*, 1965, **121**, 158-164.
2. G. M. Loiacono, J. F. Balascio, R. Bonner and A. Savage, *J. Cryst. Growth*, 1974, **21**, 1-11.
3. F. A. Danevich, B. V. Grinyov, S. Henry, M. B. Kosmyna, H. Kraus, N. Krutyak, V. M. Kudovenko, V. B. Mikhailik, L. L. Nagornaya, B. P. Nazarenko, A. S. Nikolaiko, O. G. Polischuk, V. M. Puzikov, A. N. Shekhovtsov, V. I. Tretyak and Y. Y. Vostretsov, *Nucl. Instrum. Meth. A*, 2010, **622**, 608-613.
4. A. Kudo, M. Steinberg, A. J. Bard, A. Campion, M. A. Fox, T. E. Mallouk, S. E. Webber and J. M. White, *Catal. Lett.*, 1990, **5**, 61-66.
5. M. Shen, Q. Zhang, H. Chen and T. Peng, *CrystEngComm*, 2011, **13**, 2785-2791.
6. K. M. Nam, H. S. Park, H. C. Lee, B. H. Meekins, Kevin C. Leonard and A. J. Bard, *J. Phys. Chem. Lett.*, 2013, **4**, 2707-2710.
7. G.-J. Xing, R. Liu, C. Zhao, Y.-L. Li, Y. Wang and G.-M. Wu, *Ceram. Int.*, 2011, **37**, 2951-2956.
8. M. Hashim, C. Hu, X. Wang, X. Li and D. Guo, *Appl. Surf. Sci.*, 2012, **258**, 5858-5862.
9. H. Kadowaki, N. Saito, H. Nishiyama, H. Kobayashi, Y. Shimodaira and Y. Inoue, *J. Phys. Chem. C* 2007, **111**, 439-444.
10. H. Fu, C. Pan, L. Zhang and Y. Zhu, *Mat. Res. Bull.*, 2007, **42**, 696-706.
11. D. B. Hernández-Uresti, A. Martínez-de la Cruz and J. A. Aguilar-Garib, *Catalysis Today*, 2013, **212**, 70-74.
12. A. Martínez-de la Cruz, D. B. Hernández-Uresti, L. M. Torres-Martínez and S. W. Lee, *Reac. Kinet. Mech. Cat.*, 2012, **107**, 467-475.
13. K. Dai, Y. Yao, H. Liu, I. Mohamed, H. Chen and Q. Huang, *J. Mol. Catal. A: Chem.*, 2013, **374-375**, 111-117.
14. T.-H. Kim, Y.-H. Jo, G. Gyawali, R. Adhikari, T. Sekino and S.-W. Lee, *Mater. Lett.*, 2013, **101**, 99-102.
15. Y. Zhang, N. A. W. Holzwarth and R. T. Williams, *Phys. Rev. B*, 1998, **57**, 12738-12750.
16. C. Jianyu, Z. Qiren, L. Tingyu, S. Zexu and P. Chunying, *Comput. Mater. Sci.*, 2008, **41**, 330-333.
17. M. Fujita, M. Itoh, H. Mitani and S. Tyagi, *Phys. Status Solidi B*, 2010, **247**, 405-410.
18. J. Bi, L. Wu, Y. Zhang, Z. Li, J. Li and X. Fu, *Appl. Catal. B: Environ.*, 2009, **91**, 135-143.
19. J. C. Szancoski, M. D. R. Bomio, L. S. Cavalcante, M. R. Joya, P. S. Pizani, J. A. Varela, E. Longo, M. S. Li and J. A. Andrés, *J. Phys. Chem. C*, 2009, **113**, 5812-5822.
20. M. R. D. Bomio, L. S. Cavalcante, M. A. P. Almeida, R. L. Tranquilin, N. C. Batista, P. S. Pizani, M. Siu Li, J. Andres and E. Longo, *Polyhedron*, 2013, **50**, 532-545.
21. J. Chen, Q. Zhang, T. Liu, Z. Shao and C. Pu, *Nucl. Instrum. Meth. B*, 2007, **260**, 619-622.
22. W. van Loo, *J. Solid State Chem.*, 1975, **14**, 359-365.
23. I. Vesselinov, *J. Cryst. Growth*, 1996, **167**, 725-728.
24. V. M. Anandakumar and A. Khadar, *Phys. Stat. Sol. A*, 2008, **205**, 2666-2672.
25. I. S. S. Pinto and H. M. V. M. Soares, *J. Clean Prod.*, 2013, **52**, 481-487.
26. H.-L. Wang, X.-D. Ma, X.-F. Qian, J. Yin and Z.-K. Zhu, *J. Solid State Chem.*, 2004, **177**, 4588-4596.
27. A. Phuruangrat, T. Thongtem and S. Thongtem, *J. Cryst. Growth*, 2009, **311**, 4076-4081.
28. A. Phuruangrat, T. Thongtem and S. Thongtem, *Curr. Appl Phys.*, 2010, **10**, 342-345.
29. J. Geng, J.-J. Zhu and H.-Y. Chen, *Cryst. Growth. Des.*, 2006, **6**, 321-326.
30. E. E. Chao and K. L. Cheng, *Talanta*, 1977, **24**, 247-250.
31. P. Kwolek, T. Łokcik, T. Tokarski and K. Szacilowski, *Arch. Metall. Mater.*, 2013, **58**, 217-222.
32. M. Buchalska, P. Łabuz, Ł. Bujak, G. Szewczyk, T. Sarna, S. MacKowski and W. MacYk, *Dalton Transactions*, 2013, **42**, 9468-9475.
33. M. J. Frisch, G. W. Trucks, H. B. Schlegel, G. E. Scuseria, M. A. Robb, J. R. Cheeseman, G. Scalmani, V. Barone, B. Mennucci, G. A. Petersson, H. Nakatsuji, M. Caricato, X. Li, H. P. Hratchian, A. F. Izmaylov, J. Bloino, G. Zheng, J. L. Sonnenberg, M. Hada, M. Ehara, K. Toyota, R. Fukuda, J. Hasegawa, M. Ishida, T. Nakajima, Y. Honda, O. Kitao, H. Nakai, T. Vreven, J. A. Montgomery Jr., J. E. Peralta, F. Ogliaro, M. Bearpark, J. J. Heyd, E. Brothers, K. N. Kudin, V. N. Staroverov, R. Kobayashi, J. Normand, K. Raghavachari, A. Rendell, J. C. Burant, S. S. Iyengar, J. Tomasi, M. Cossi, N. Rega, J. M. Millam, M. Klene, J. E. Knox, J. B. Cross, V. Bakken, C. Adamo, J. Jaramillo, R. Gomperts, R. E. Stratmann, O. Yazyev, A. J. Austin, R. Cammi, C. Pomelli, J. W. Ochterski, R. L. Martin, K. Morokuma, V. G. Zakrzewski, G. A. Voth, P. Salvador, J. J. Dannenberg, S. Dapprich, A. D. Daniels, O. Farkas, J. B. Foresman, J. V. Ortiz, J. Cioslowski and D. J. Fox, *Gaussian 09, Rev. A.02*, Gaussian, Inc., Wallingford CT, 2009.
34. A. Nicklass, M. Dolg, H. Stoll and H. Preuss, *J. Chem. Phys.*, 1995, **102**, 8942-8952.
35. T. Araki, *Memoirs Coll. Sci. Univ. Kyoto*, 1957, **24**, 155-160.
36. G. Kortüm, *Reflectance spectroscopy Principles, Methods and Applications*, Springer-Verlag, Berlin Heidelberg New York, 1969.
37. T. P. McLean, in *Progress in Semiconductors*, ed. A. F. Gibson, Heywood & Company Ltd., London, 1960.
38. L. Brus, *J. Phys. Chem.*, 1986, **90**, 2555-2560.
39. M. D. Volnianskiy, A. Y. Kudzin, S. N. Plyaka and Z. H. Balasmeh, *Phys. Stat. Sol. B*, 2005, **242**, 1349-1353.
40. A. Podborska, B. Gawel, Ł. Pietrzak, I. B. Szymańska, J. K. Jeszka, W. Łasocha and K. Szacilowski, *J. Phys. Chem. C*, 2009, **113**, 6774-6784.
41. B. A. Boukamp, *J. Electrochem. Soc.*, 1995, **142**, 1885-1894.
42. B. A. Boukamp, *Solid State Ionics*, 2004, **169**, 65-73.
43. M. A. Orazem and B. Tribollet, *Electrochemical impedance spectroscopy*, John Wiley & Sons, Hoboken, New Jersey., 2008.
44. P. Kwolek and K. Szacilowski, *Electrochim. Acta*, 2013, **104**, 448-453.
45. J. Mech, M. A. Grela and K. Szacilowski, *Dyes Pigments*, 2014, **103**, 202-213.

-
46. W. R. Duncan and O. V. Prezhdo, *J. Phys. Chem. B*, 2005, **109**, 365-373.
47. W. R. Duncan, W. M. Stier and O. V. Prezhdo, *J. Am. Chem. Soc.*, 2004, **127**, 7941-7951.
- 5 48. M. X. Tan, P. E. Laibinis, S. T. Nguyen, J. M. Kesselman, C. E. Stanton and N. S. Lewis, *Prog. Inorg. Chem.*, 1994, **41**, 21-144.
49. S. Gawęda, R. Kowalik, P. Kwolek, W. Macyk, J. Mech, M. Oszajca, A. Podborska and K. Szaciłowski, *Isr. J. Chem.*, 2011, **51**, 36-55.
50. M. Wojnicki, T. Tokarski and P. Kwolek, *Arch. Metall. Mater.*, 2013,
10 **58**, 709-716.
51. R. Memming, *Semiconductor electrochemistry*, Wiley-VCH, Weinheim, 2001.
52. P. Kwolek, K. Pilarczyk, T. Tokarski, K. Lewandowska and K. Szaciłowski, *Nanoscale*, 2014, **6**, 2244-2254.
- 15 53. A. Paulenova, S. E. Creager, J. D. Navratil and Y. Wei, *J. Power Sources*, 2002, **109**, 431-438.
54. D. Pletcher and E. M. Valdes, *Electrochim. Acta*, 1988, **33**, 499-507.



The well-known material exhibits novel properties.
98x50mm (300 x 300 DPI)